Official journal of the CIOMP 2047-7538
www.nature.com/lsa

ARTICLE Open Access

Observation of a single protein by ultrafast X-ray diffraction

Tomas Ekeberg[1], Dameli Assalauova[2], Johan Bielecki[3], Rebecca Boll[3], Benedikt J. Daurer[4], Lutz A. Eichacker[5], Linda E. Franken[6], Davide E. Galli[7], Luca Gelisio[2], Lars Gumprecht[8], Laura H. Gunn[1,9], Janos Hajdu[1], Robert Hartmann[10], Dirk Hasse[1], Alexandr Ignatenko[2], Jayanath Koliyadu[3,11], Olena Kulyk[12], Ruslan Kurta[3], Markus Kuster[3], Wolfgang Lugmayr[13,14], Jannik Lübke[8,15,16], Adrian P. Mancuso[3,17], Tommaso Mazza[3], Carl Nettelblad[18], Yevheniy Ovcharenko[3], Daniel E. Rivas[3], Max Rose[2], Amit K. Samanta[8], Philipp Schmidt[3], Egor Sobolev[3,19], Nicusor Timneanu[20], Sergey Usenko[3], Daniel Westphal[1], Tamme Wollweber[15,16,21,22], Lena Worbs[8,16], Paul Lourdu Xavier[3,8,21], Hazem Yousef[3], Kartik Ayyer[15,21,22], Henry N. Chapman[8,15,16], Jonas A. Sellberg[11], Carolin Seuring[13,23], Ivan A. Vartanyants[2], Jochen Küpper[8,15,16], Michael Meyer[3] and Filipe R. N. C. Maia[1,24]✉

Abstract

The idea of using ultrashort X-ray pulses to obtain images of single proteins frozen in time has fascinated and inspired many. It was one of the arguments for building X-ray free-electron lasers. According to theory, the extremely intense pulses provide sufficient signal to dispense with using crystals as an amplifier, and the ultrashort pulse duration permits capturing the diffraction data before the sample inevitably explodes. This was first demonstrated on biological samples a decade ago on the giant mimivirus. Since then, a large collaboration has been pushing the limit of the smallest sample that can be imaged. The ability to capture snapshots on the timescale of atomic vibrations, while keeping the sample at room temperature, may allow probing the entire conformational phase space of macromolecules. Here we show the first observation of an X-ray diffraction pattern from a single protein, that of *Escherichia coli* GroEL which at 14 nm in diameter is the smallest biological sample ever imaged by X-rays, and demonstrate that the concept of diffraction before destruction extends to single proteins. From the pattern, it is possible to determine the approximate orientation of the protein. Our experiment demonstrates the feasibility of ultrafast imaging of single proteins, opening the way to single-molecule time-resolved studies on the femtosecond timescale.

Introduction

X-ray free-electron lasers (XFEL) have transformed the study of ultrafast phenomena at the atomic level, from transient room-temperature superconductivity[1] to the fastest processes following water ionisation[2]. This has also been the case in structural biology with the birth of serial femtosecond crystallography (SFX)[3] and more recently the development of time-resolved SFX[4]. Yet the requirement of crystals is limiting as demonstrated by the spectacular development in cryo-electron microscopy (cryo-EM)[5]. More importantly, the need to synchronise all unit cells in a crystal makes photo-activation the only feasible trigger for ultrashort timescales. It also prevents the observation of individual molecular behaviour, e.g., multiple conformations. Currently, cryo-EM is the method of choice for high-resolution single-molecule time-resolved

Correspondence: Filipe R. N. C. Maia (filipe.maia@icm.uu.se)
[1]Laboratory of Molecular Biophysics, Department of Cell and Molecular Biology, Uppsala University, Husargatan 3 (Box 596), SE-75124 Uppsala, Sweden
[2]Deutsches Electronen-Synchrotron DESY, Notkestrasse 85, 22607 Hamburg, Germany
Full list of author information is available at the end of the article

studies, but it is limited to millisecond timescales due to the time it takes to freeze the sample and collect the data[6]. By bypassing these limitations, femtosecond X-ray diffractive imaging (FXI)[7] has the potential to observe single-molecules with sub-picosecond time resolution and, due to the higher sample temperature, may allow sampling from a broader conformational landscape.

The chaperonin GroEL is an abundant molecular chaperone and, together with its cofactor GroES, is important in the folding of a large range of proteins[8]. *Escherichia coli* GroEL is a 14-mer formed by two heptameric subunit rings[9], totalling ~800 kDa and arguably the most studied chaperonin. It was also one of the first large macromolecular complexes to be successfully measured by native mass spectrometry[10] and is nowadays often used as a benchmark to demonstrate the resolution of new systems[11–13]. Its size and availability also made it an early target for single-particle cryo-EM studies[14,15]. These characteristics along with the extensive body of available knowledge and distinctive shape, recognisable even at low resolution, make GroEL an ideal prototype system for single-particle X-ray diffraction.

Despite continuous progress in FXI[16–19], no single-protein diffraction has ever been measured, and studies have been limited to more strongly diffracting samples, such as viruses[20] and cells[21]. In this paper, we present the first interpretable X-ray diffraction signal from a protein complex, the chaperonin GroEL, an order of magnitude lighter than the smallest biological sample previously reported[22], the ~9 MDa Tomato bushy stunt virus. With it we demonstrate the principle of diffraction before destruction[23] at the protein scale. This opens the doors to ultrafast studies on single-protein molecules making use of the extraordinary brightness and time resolution of XFELs.

Results

The experiment was performed at the Small Quantum Systems (SQS) scientific instrument of the European XFEL (EuXFEL) facility in Schenefeld, Germany[24]. GroEL particles were exposed to femtosecond soft X-ray pulses from the EuXFEL at a photon energy of 1200 eV and an average pulse energy of 6.5 mJ.

Individual GroEL particles, characterised by a differential mobility analyzer (DMA) (Supplementary Fig. S1) and cryo-EM (Supplementary Figs. S2–S5), were transferred from solution to the gas phase using an electrospray setup[22] in which a charged jet of the sample in liquid generated droplets of around 110 nm in diameter in the presence of an inert gas mixture of CO_2 and N_2 surrounding the jet (Fig. 1). These droplets were then neutralised and focused through an aerodynamic lens[25] creating a thin stream of particles. Most or all of the volatile buffer solution evaporated during the process and a stream of mostly dry particles reached the interaction region.

Diffraction data were collected with a pnCCD detector consisting of two detection planes[26] placed 150 mm downstream of the interaction region (Fig. 1). The resolution limit of this setup is 4 nm due to the detector's numerical aperture. Only a small fraction of the X-ray pulses will intersect with one of the injected particles in what is called a hit. The majority of the detector readouts therefore only contain background, which arises mainly from the injection gas but also from the beamline itself.

The gas used in the electrospray injection setup created two types of experimental background: fluorescence and elastically scattered photons. The fluorescence has a photon energy of 277, 392 and 525 eV, respectively, from the carbon, nitrogen and oxygen Kα1-shell, compared to the incoming photons of 1200 eV. The energy resolution of the pnCCD detector of 40 eV[27] allows us to discriminate between the fluorescence and elastic scattering for all pixels that receive at most one photon (Supplementary Fig. S6), a condition that was generally fulfilled in this experiment.

In contrast to the fluorescence background, it was not possible to filter out the elastic scattering from the gas since it has the same photon energy as the signal. The same is also true for the so-called beamline background—photons resulting from the interaction of the X-rays with elements of the beamline. To quantify the different sources of background we collected data both with the injection off and the injection turned on but without a supply of sample. This showed that the injection gas contributed on average 17,600 photons per diffraction pattern, compared to the beamline contribution of only 86 photons per diffraction pattern on average (Fig. 2).

The EuXFEL delivers its pulses in 10 pulse trains per second and with a MHz repetition rate within each train[24,28]. Because a detector based on CCD technology is not capable of providing an MHz image readout rate within the pulse train, we were limited to one readout per train, which severely limited the data collection rate. As a consequence, from 84,000 readouts only 816 patterns matched our initial hit-detection (see Methods for details). In Fig. 3a we can see the number of photons in each of these patterns. Further inspection reveals that most of the major peak is actually non-hits caused by stochastic variations in the background triggering our hit-detection. The 172 patterns that contain a signal that is larger than 19,000 photons do however mostly consist of actual hits. We compared the diffraction of spheres of different sizes to the patterns to identify their most likely size. The size histogram for all patterns with more than 19,000 photons is shown in Fig. 3b. The histogram peaks at 15 nm which matches the expected size of GroEL with very few particles of smaller sizes

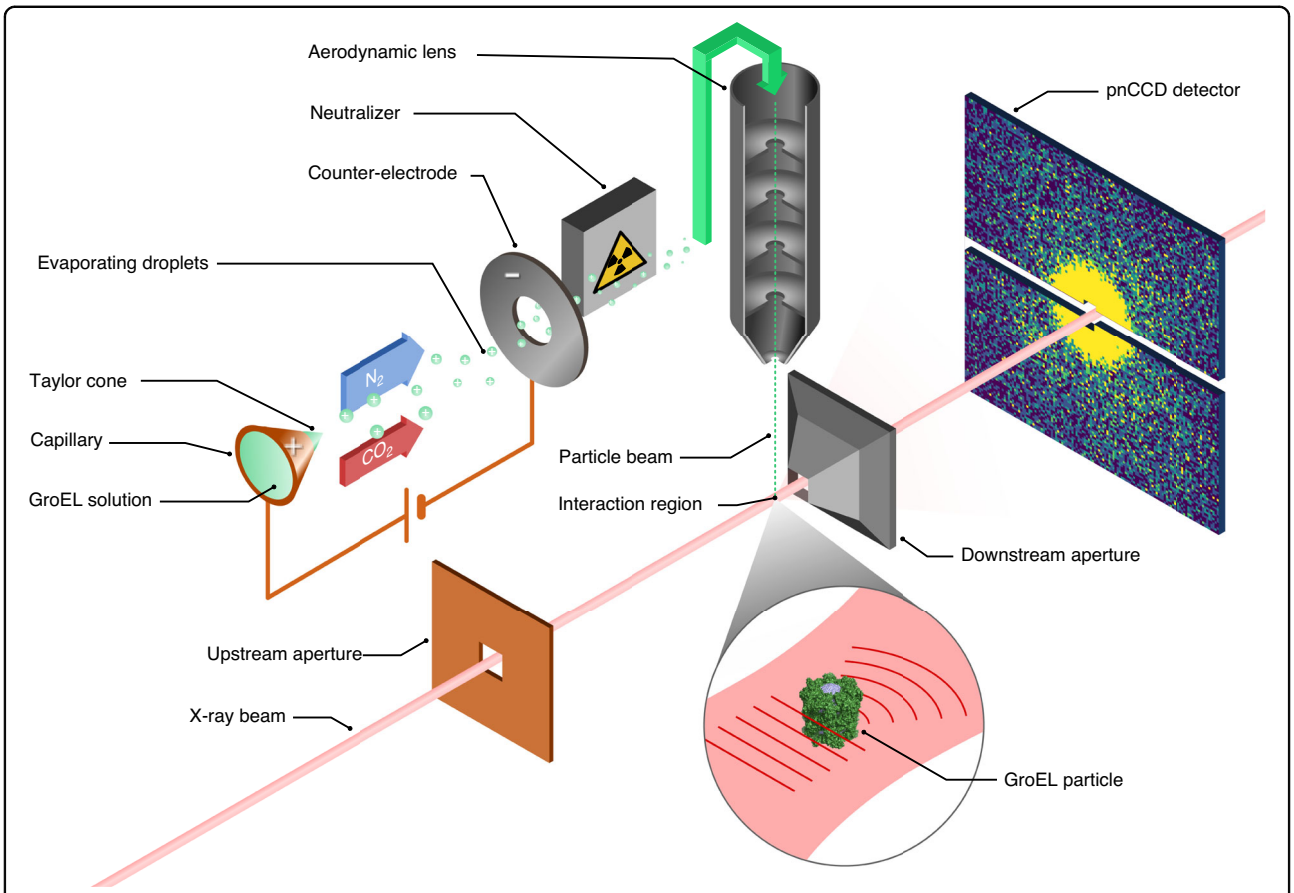

Fig. 1 Experimental setup. A solution containing GroEL particles, each roughly a cylinder 14 nm in diameter and height, is aerosolized, using electrospray ionisation followed by neutralisation, and focused into a thin stream using an aerodynamic lens. The stream is then intersected with the path of the XFEL beam and the diffracted signal is collected on a pair of pnCCD detectors downstream of the interaction region. To minimise the amount of background, the beam is cleaned up by apertures both before and after the interaction region[53]

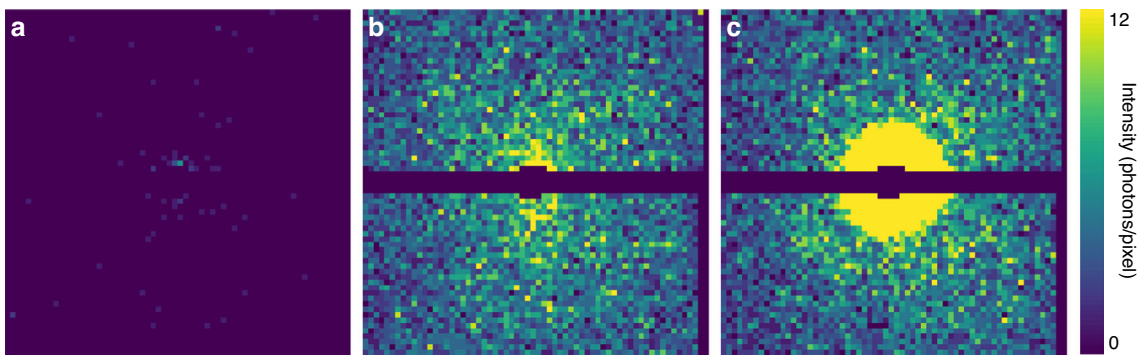

Fig. 2 Experimental diffraction data. a Average beamline background, i.e., background with gas from injection turned off, plotted after Poisson sampling. **b** Average measured background, plotted after Poisson sampling. **c** Measured single diffraction pattern of a single GroEL particle. All patterns are downsampled to 64 × 64 to make features more visible on this figure. In (**a**) and (**b**), Poisson sampling is used to make the patterns comparable with the single pattern shown in (**c**)

than this. As expected, there is a longer tail towards larger sizes that most likely contains samples with aggregations of either water, salt or broken proteins, and towards the end of the tail, clusters of several GroEL complexes. Inspection shows that the small peak below 5 nm does not originate from our sample but is made up of strong background shots and all have photon counts lower than 20,500.

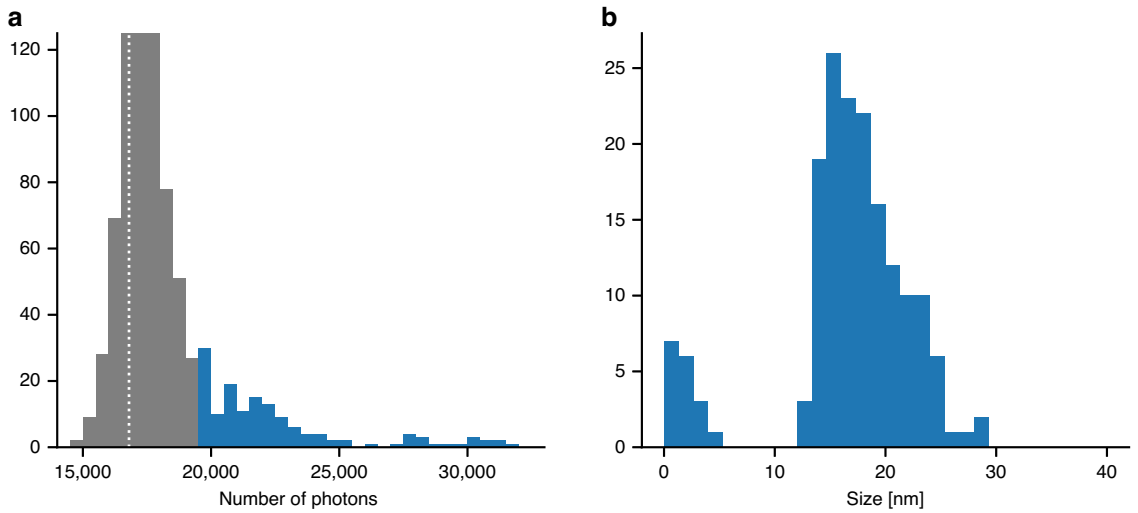

Fig. 3 Data classification. a Histogram showing the number of photons per pattern. The dotted line marks the average strength of the background. The strong peak around 17,000 contains mainly pure-background shots, but most diffraction patterns above 19,000, marked in blue, have diffraction signal from a sample. **b** Histogram of the size of the sample in all patterns with more than 19,000 photons. The peak at 15 nm matches the size of GroEL and the second smaller peak below 5 nm consists of particularly strong pure-background shots

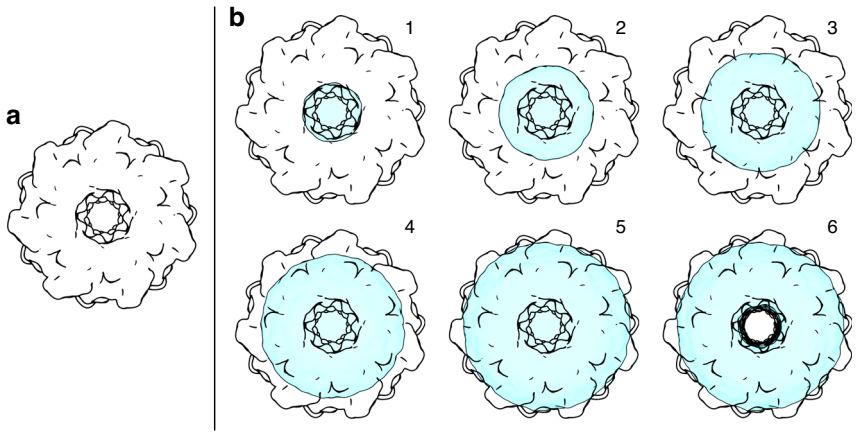

Fig. 4 Density models. The original structure (**a**) and six models with added density (**b**) were compared to the recorded diffraction intensity. The density is modelled as water. The weight of water, in relation to the weight of the protein, for models 1–6 is 13%, 24%, 37%, 51%, 69% and 54% respectively. All models fill the hollow core of GroEL except for model 6

To further verify that the collected diffraction is indeed from GroEL samples, we will focus our analysis to a single diffraction pattern with the combination of a very high signal-strength and favourable orientation that made it deviate from the spherical symmetry (Fig. 2c). The deviation from the circular symmetry in the first fringe is clear and consistent with the barrel-shaped structure of GroEL. To verify that the pattern originates from a GroEL particle, we compared it with simulated diffraction data from the structure of GroEL, shown in Fig. 4a, determined by X-ray crystallography[29]. This comparison does however have three problems: (1) the orientation of the molecule that gave rise to our pattern is unknown; (2) the centre of the diffraction pattern is uncertain; (3) our diffraction data is a combination of signal and background.

We addressed problems (1) and (2) by applying a template matching scheme where many diffraction patterns were simulated in orientations sampling the full three-dimensional diffraction space with an accuracy of 7 degrees. These patterns were then translated both horizontally and vertically to cover the different possible centre positions. In total, the experimental pattern was compared to 4.3 million simulated and translated patterns.

To handle problem (3), we first summed up the average background from one of the runs where gas but no

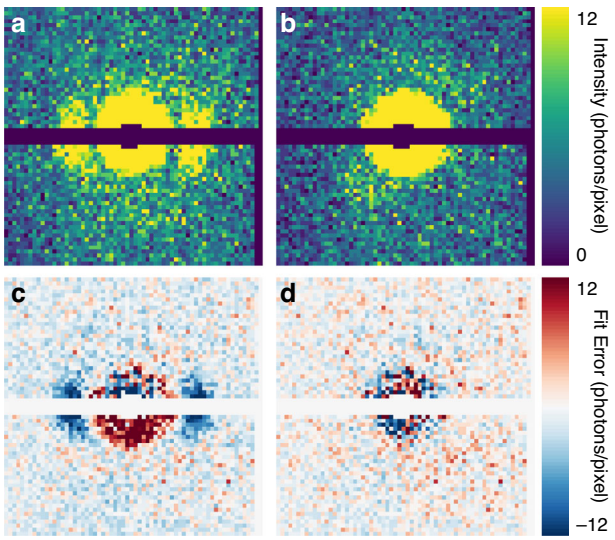

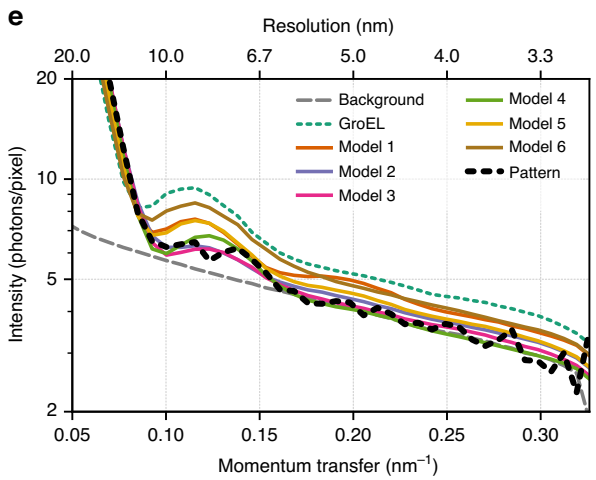

Fig. 5 Pattern comparisons. a Simulated diffraction from the dry GroEL particle in the orientation that best matches the measured pattern. Patterns are plotted after Poisson sampling to make the patterns comparable with the single pattern shown in Fig. 2c. **b** A significantly better fit is achieved from density model 3. **c**, **d** Fit error between the measured pattern compared to **c** the simulated diffraction from the dry GroEL particle and **d** model 3. **e** Radial average of the background to illustrate the difference between the models, the best-fitting diffraction from the crystal structure of GroEL (dotted green line), each density model (solid coloured lines) and the measured pattern (dotted black line). The dry molecule predicts too much intensity outside of the central speckle, whereas water models 2, 3 and 4 follow the data much closer. The images (**a**–**d**) and the pixels of (**e**) correspond to 64 × 64 downsampled patterns

sample was injected. For each comparison under the template matching, the pattern was fitted to a linear combination of the average background and the template pattern. The best-fitting background-template combination is shown in Fig. 5a.

Even this best-fitting background-template combination does not match the experimental pattern very well. The sum of the residual error between the pattern and the simulation is 180 photons compared to 143 photons which would have been expected if Poisson noise was the only cause for the discrepancy. A hint at an explanation can be found by observing that the first fringe in the simulation is significantly stronger than in the experimental pattern. This indicates that the simulation has too many low-resolution, high-contrast elements. This suggests that the hollow centre of the barrel-shaped protein in the simulation is fully or partially filled in the particle that gave rise to the pattern.

We identify three possible origins for this density: (1) It is possible that not all of the water evaporated from the sample during injection, in particular water molecules that are less exposed to the surface. (2) 2D class averages from our cryo-EM measurements (Supplementary Fig. S4) show some density inside the barrel higher than the surrounding water. This density is most likely protein. (3) Depending on the size of the initial solvent droplet there will be a considerable amount of contaminants left on the sample after evaporation. This contributes to the peak at 11 nm observed in DMA data (Supplementary Fig. S1) and could explain the extra density. At the resolution available in this experiment, we cannot determine if any of these hypotheses is correct. We can, however, test the theory that extra density within the centre of the protein can explain the observed data.

To do this, we created six different density models (Fig. 4) by adding varying amounts of water to the hollow centre or the surrounding groves in the protein. We then repeated the template matching with each of them, knowing that similar models filled with broken proteins or salt would give indistinguishable results. Five of the models fill up the hollow core of the protein at varying proportions, which is what our earlier interpretation of the data suggests. As a control, we also include a density model where only the barrel edges are hydrated and the core is empty.

The radial average of the pattern and the best fit for the different density models showed a better fit for all new models compared to the original structure, with models 2, 3 and 4 giving the best results (Fig. 5e). The total residual error between the simulation and the experimental pattern also confirmed that model 3 was the best fit with an error of 160 photons. The simulation from model 3 is shown in Fig. 5b and the oriented model is shown in Supplementary Fig. S7. The signal in the radial average of the pattern drops down to the background level at a resolution of about 6 nm. We also performed phase

retrieval of the pattern (Supplementary Fig. S10) but the resulting map is of too low resolution to allow any further conclusions to be drawn.

We then checked if the hydrated model was supported by the rest of our data. We summed up all the patterns with sizes between 10 and 20 nm from the histogram shown in Fig. 3b, excluding the strong one shown in Fig. 2c. The resulting virtual powder pattern is in strikingly good agreement with the simulated powder diffraction from a hydrated GroEL, unlike for a dry GroEL particle or a water sphere (Supplementary Fig. S11).

Not only are these results consistent with diffraction from a GroEL molecule, which is the first example of interpretable X-ray diffraction being collected from a single protein, but they also suggest that the aerosolized GroEL particle contained an extra density in the otherwise hollow centre at the time of interaction.

The overall size and shape of our sample match that of the crystal structure quite well, unlike earlier studies using a combination of ion mobility analysis and mass spectrometry[30] which have observed an unusually high compaction of GroEL in the gas phases. The difference is likely due to the different experimental conditions. In our case GroEL was quickly neutralised after electrospray and not actively dried, while the compaction was seen for dry particles with charges up to $z = 70$, which is likely to affect the structure. This suggests that hydration and charge state are important to preserve the GroEL structure in FXI experiments.

From our modelling, we also concluded that of the 30,500 photons in the pattern, only 13,800 originated from the sample and 16,700 originated from the background scattering. This highlights the importance of continued efforts to further reduce background scattering from the injection gas in such experiments.

The pattern fittings showed that the photon fluence at the sample was 280 μJ/μm^2. This aligns well with the maximum fluence expected from the pulse given a measured pulse energy of 6.6 mJ before the focusing optics and the focus profile and transmission of the beamline (see Methods). It suggests that this particular GroEL molecule interacted with a region of the pulse that was almost at the peak.

Discussion

When the first XFELs were constructed, one of the main promises was the prospect of diffraction studies of single proteins using the so-called "diffraction before destruction method" that could take advantage of the ultrafast time resolution enabled by this new generation of light sources. However, concerns were raised on whether the proteins' structure would survive the transition to the gas phase and, even if it did, whether the signal would be strong enough to be visible above the background noise. In this paper, we have been able to address these concerns by reporting the first X-ray diffraction pattern collected from a single protein.

The signal in this pattern is weak, but the distinct geometry of the GroEL complex is distinguishable above the background noise. Furthermore, the signal matches well with the predicted signal from a model of GroEL with extra density added to the central cavity. At this resolution, it cannot be determined if the extra density is made up of water or something else.

Simulations have shown that residual water molecules are vital for the stability of proteins in the gas phase[31]. A significant amount of water attached to GroEL in our experiment would, without doubt, contribute to keeping its structure preserved during the transition to the gas phase. It was recently shown to be possible to obtain high-resolution structures of proteins after they have been electrosprayed and soft-landed on a cryo-EM grid[32]. The resulting structure is relatively similar to the one in solution, despite the particles having been dried and charged. Still, the amount of solvent remaining after electrospray is likely to be crucial to determine how close the conformational landscape of the protein is to the one in its native conditions. The presence of water around the sample is also predicted to delay radiation damage to the sample by acting as a sacrificial tamper[33]. Large amounts of solvent might introduce problems for 3D orientation recovery and subsequent merge of a large dataset. These problems will however be limited to the same resolution as the size of the fluctuations in solvent distribution between the samples, which for water is expected to be small[34].

The factors that currently prevent FXI from determining full 3D structures are the low signal-to-noise ratio due to the strong background and the low data rate. Since most of the background originated from the injection gas, we identify this as a major target for future development. Potentially, better shielding of the gas and a transition to a low-Z alternative such as helium could improve the signal-to-background ratio by more than tenfold. The availability of a 4.5 MHz DSSC imaging detector of megapixel size[35] at the SQS instrument will allow us to exploit the 4.5 MHz pulse repetition frequency within one pulse train of the XFEL, yielding multiple opportunities for a hit in each pulse train. Furthermore, the vetoing capability[36,37] of the DSSC detector has the potential to improve the fraction of interpretable diffraction images from a few per cent to around 30% when EuXFEL is running at its full capacity of 27 kHz.

Here we have presented the first interpretable X-ray diffraction pattern from a single protein, frozen in time by the femtosecond X-ray pulse, and experimentally demonstrated that the concept of diffraction before destruction extends to single proteins. This single pattern

represents an important step towards solving 3D protein structures with the method of diffraction before destruction and shows that several of the hurdles can indeed be overcome. With higher data rates, many such patterns can map out the structure and function of dynamic proteins with the staggering time resolution enabled by XFELs.

Materials and methods

Beamline and instrument setup

The EuXFEL was tuned to a photon energy of 1200 eV corresponding to a wavelength of 1.03 nm. The focus size was estimated to be 2 μm × 2 μm based on wavefront sensor measurements (Supplementary Fig. S8). The total energy of each X-ray pulse was measured before any beamline optical element using one of the X-ray gas detectors available at the beamline[38] and found to hover around 6.5 mJ. Using the wavefront sensor measurements (Supplementary Fig. S8), we estimated the fluence at the interaction region. We assumed that the field of view of the sensor captures the vast majority of the photons present in the beam. Using the measured pulse energy and a beamline transmission of 46% (measured subsequently), we estimated the maximum fluence across the sensor for each of the five different wavefront measurements. The average of those estimates was 232 ± 62 μJ/μm^2. The XFEL was run at one pulse per train giving a repetition rate of 10 Hz.

Sample injection

Individual proteins were transferred into the gas phase and transported into the X-ray interaction region as described in Bielecki et al.[22]. The sample solution consisted of GroEL proteins with a concentration of about 150 nM in an ammonium acetate buffer. Nebulization of the protein solution took place with an electrospray nozzle which produces initial droplets with diameters between 80 and 400 nm depending on the sample flow rate. The charged droplets emanating from the electrospray nozzle were neutralised by an X-ray source (Hamamatsu L12645) that ionised the sheath gas transporting the droplets.

The electrospray capillary had an inner diameter of 40 μm, an outer diameter of 360 μm, and the sample flow rate was adjusted by controlling the overpressure in the sample compartment with a remotely controllable differential pressure regulator (Bronkhorst P-506C-4K0D-TGD-33-V delta P pressure gauge controlling an F-001AI-IIU-33-V regulating valve). The tip of the capillary had been ground to a 30-degree cone with a final tip diameter of 100 μm. The droplet diameter could be controlled from 80 nm at 0.25 psi overpressure to 400 nm at 10 psi overpressure.

Monodispersity and size of the sample after nebulisation were both monitored before, and during the measurements, with an SMPS (TSI SMPS 3938) consisting of a DMA coupled to a condensation particle counter. To minimise the salt layer on the sample surface, while still maintaining a stable Taylor cone, an overpressure of 1 psi had to be applied to the sample reservoir used, resulting in initial droplets with a diameter of approximately 110 nm.

The neutralised droplets were transported into the X-ray interaction region through an aerodynamic lens, creating a particle beam as described in Hantke et al.[25]. Excessive gas flow from running the electrospray was removed in two skimmer stages. As a result, the 1 bar pressure at the electrospray was reduced to 30 mbar after the first skimmer, and the entrance pressure to the aerodynamic lens was 0.6 mbar after the second skimmer stage.

The beam of injected particles was intercepted by the pulse train of the XFEL. To optimise the position of the particle beam, a sucrose solution was injected, creating tiny sucrose spheres, and the hit rate on the spheres was used as a feedback parameter[39].

Detector and data processing

Diffraction data were collected with the EuXFEL pnCCD detector[26] running in high-gain mode. This setup allows for a maximum full-period resolution of 4 nm determined by the scattering-angle at the edge of the detector. Since the detector cannot keep up with the pulse frequency within the pulse trains, we were limited to the 10 Hz frequency of the pulse trains themselves. Each pnCCD sensor panel is made up of a grid of 512 × 1024 pixels each with a size of 75 μm × 75 μm. The two panels were both placed 15 cm downstream of the interaction region and with a gap of 3.7 mm to allow the direct beam to pass through. The exact translation of the detector panels was optimised using strongly diffracting sucrose particles and the understanding that this diffraction adheres to Friedel symmetry.

Detector readout baseline, called pedestal data, were collected regularly throughout the experiment when the beam was off and were subtracted from each readout. In addition, a common mode correction was applied to each line of each detection plane for each individual image. This correction is performed by subtracting the median of the pixel values in each line from all values of the same line and is possible when the photon density is low, like in our case.

The slope of the relation between photon energy and ADU of each detector pixel, called the gain, varies slightly from line to line since each line has its own amplifier. In addition, along a line, the measured energy might decline due to the charge transfer inefficiency. To handle both these effects we determined a unique gain for each pixel. This value was found by constructing a histogram of the

signal detected in all images in a particular pixel (Supplementary Fig. S6) and subsequently fitting a Gaussian function to the peak corresponding to zero photons and subsequently fitting another Gaussian function to the much smaller peak corresponding to a single photon. The distance between the peaks must then correspond to the photon energy of 1200 eV.

The detector signal provided in units of ADU was converted into photon counts by dividing each pixel readout with the gain retrieved above and rounding to its closest integer. To filter out the contribution from fluorescence in the range from 200 to 600 eV readout values up to 900 eV were rounded down to zero instead of up.

For each readout, the number of lit pixels was calculated as the number of pixels with a photon count of 3 or higher. Hits were identified as any readout where the number of lit pixels was larger than 16.

The average background was estimated from 32,000 readouts (Supplementary Fig. S9) where the injector was running but without any sample, thus including the contribution of the scattering from the gas used for injection.

Before analysis, each diffraction pattern was downsampled to a size of 128 × 128 pixels. The downsampling was done after the conversion to discrete photons since the combined readout noise in one superpixel would otherwise be much larger than the photon energy. Additional downsampling to a final size of 64 × 64 was performed before plotting to make the features of the diffraction patterns clearer.

Water models were generated by solvating the GroEL structure (PDB entry 1SS8[29]) using the gmx solvate function in GROMACS[40]. Water molecules were removed if they fell outside of a cylinder of varying size. The top and bottom of the cylinders were also pruned to match the shape of the protein. The code for generating these models and the PDB files for them are made available (see Code availability).

Template diffraction patterns were simulated with Condor[41] using the wavelength and detector geometry from the experiment. The output without Poisson noise was used in the further analysis. The protein orientations were distributed evenly in rotation space by choosing quaternions that evenly sample the cells of the 600-cell, similarly to Loh et al.[42]. Each edge in the 600-cell was subdivided 8 times, which yields 25,680 different orientations and corresponds to an angle of 6.8 degrees between adjacent orientations. The simulated patterns were then translated both horizontally and vertically, in a 13 × 13 pixel search grid, to cover the different possible centre positions, which arises due to the pointing uncertainty of the X-rays. This resulted in a total of 4,339,920 simulated patterns for each model structure.

For the template matching, each template was combined with the average background with a variable scaling term for the fluence of the signal and background, respectively. These scaling terms were used as fitting parameters in a least-square optimisation implemented in the scipy function leastsq[43]. The goodness of fit was then compared between all templates to identify the best orientation.

The residual error, E, or goodness of fit, is defined as

$$E = \sum_i (sS_i + bB_i - K_i)^2$$

where i is the pixel index and S is the simulated template, B is the average measured background and K is the measured pattern. The parameters s and b are the fitting parameters and describe respectively the intensity of the pulse at the sample and total intensity of the pulse.

Sample purification

Lyophilised *E. coli* GroEL (C7688) was purchased from Sigma–Aldrich (Solna, Sweden), purified and prepared for electrospray injection as described in Freeke et al.[44], but with no acetone precipitation step and with one step of size exclusion chromatography.

Characterisation of GroEL samples by DMA

The stability of GroEL against dissociation was determined using DMA combined with the same electrospray conditions as the particle injection for the main experiment. Here, a narrow peak at 16 nm was recorded which suggests that GroEL is stable under the XFEL injection conditions. A second larger peak was also detected at a smaller diameter that corresponds to contaminants from empty droplets aggregating to a ball (Supplementary Fig. S3).

Characterisation of GroEL samples by cryo-EM

For cryo-EM, vitrified grids were prepared by applying 4 µl of the GroEL sample onto glow-discharged, 200 mesh R2/2 Quantifoil grids, blotted for 4 s at blotforce 4. Grids were plunge-frozen into a 37:63 (v/v) mixture of ethane/propane cooled to liquid nitrogen temperature using a Vitrobot Mark IV instrument (Thermo Fisher Scientific) at 95% humidity and 4 °C. Samples were imaged at a nominal magnification of ×120,000 using a Talos Arctica (Thermo Fisher Scientific) transmission electron microscope operating at 200 kV accelerating voltage from a field emission gun (X-FEG) source. Movies were recorded on a Falcon 3EC electron counting direct detector (Thermo Fisher Scientific) yielding a final pixel size of 0.96 Å^2 on the specimen level. A total of 497 movies were collected in dose-fractionation mode using EPU software (Thermo Fisher Scientific) with a total dose of 40 e^-/Å^2 for each micrograph, and 1 e^-/Å^2/frame.

Cryo-EM data processing

Image processing was done in a combination of RELION 3.1[45] and cryoSPARC[46]. Movies were processed using MotionCorr 2[47] as implemented in RELION 3.1 for motion correction and gCTF[48] for CTF correction.

Cryo-EM data analysis: sample composition analysis

Laplacian picking in RELION 3.1 considers the fact that for a quality assessment, a bias-free, reference-free particle picking is needed. For this both threshold and particle size were optimised until nearly all particles, visible by eye, were picked up by the programme, and as little as possible noise was included, although some error was still present (see Supplementary Fig. S2 for an example). This resulted in a total of 47,154 particles picked with a threshold of 2 and a picked particle size between 120 and 900 Å. These particles were subsequently classified into 200 classes in cryoSPARC[46].

Only classes containing GroEL particles were submitted to heterogeneous refinement in cryoSPARC. For this, two references were supplied, one for the dual- and one for the single-ring complex. The first was an intermediate low-resolution map that was constructed during this project (see next section), aligned to D7 symmetry. The second was created based on a single-ring from the PDB structure 5W0S[49] by using the molmap function in Chimera 1.15[50] with a resolution of 20 Å. This map was subsequently resampled to the correct box and pixel size in Chimera 1.15, followed by alignment in RELION 3.1 to C7 symmetry (to centre and prepare for symmetry application). Following heterogeneous refinement, the two groups of particles were submitted to another round of 2D classification, to make sure that the separation had been thorough (see Supplementary Fig. S3). No classes belonging to the other complex were detected, but a few classes containing noise and smaller pieces of the complex were removed prior to calculating the ratio between single- and dual-ring particles in the sample. A selection of top views from the 2D classes of the dual-ring group of particles was used for Supplementary Fig. S4.

Those classes containing small proteins were 2D cleaned and the more prominent classes were subjected to initial 3D model generation in cryoSPARC. Ten low-quality 3D models were generated and they were all of similar size. Since this size was comparable to monomeric GroEL, a 3D refinement in cryoSPARC and a 3D classification in RELION 3.1 was performed. The reference was created based on a monomer from the PDB structure 5W0S by using the molmap function in Chimera 1.15 with a resolution of 20 Å. This map was subsequently resampled to the correct box and pixel size in Chimera 1.15. Neither analysis yielded a map with improved density. As the identity of these small particles is not relevant to the XFEL experiments, they were not further analysed.

Cryo-EM data analysis: high-resolution model

A deep-learning-based picking in crYOLO[51] to allow for precise picking of intact GroEL particles, resulted in a total of 14,232 particles that were imported into RELION 3.1. These were subjected to 2D classification into 50 classes and the best 10 classes were used for 3D classification into four classes with D7 symmetry in RELION 3.1. The best class included 1929 particles corresponding to the dual-ring complex and was refined with D7 symmetry and postprocessing leading to a final map resolved to 4.6 Å as shown in Supplementary Fig. S5.

Acknowledgements

We acknowledge European XFEL in Schenefeld, Germany, for provision of X-ray free-electron laser beam time at the SQS instrument and would like to thank the staff for their assistance. We acknowledge the use of the XBI biological sample preparation laboratory, enabled by the XBI User Consortium. We acknowledge valuable discussions with Erik G. Marklund. The results of the work were obtained using Maxwell computational resources operated at Deutsches Elektronen-Synchrotron (DESY), Hamburg, Germany. Part of this work was performed at the Multi-User CryoEM Facility at the Centre for Structural Systems Biology, Hamburg, supported by the Universität Hamburg and DFG grant numbers (INST 152/772-1|152/774-1|152/775-1|152/776-1|152/777-1 FUGG). We acknowledge the support of funding from: Cluster of Excellence 'CUI: Advanced Imaging of Matter' of the Deutsche Forschungsgemeinschaft (DFG) – EXC 2056 – project ID 390715994; ERC-2013-CoG COMOTION 614507; NFR 240770; Fellowship from the Joachim Herz Stiftung (P.L.X.). P.L.X. and H.N.C. acknowledge support from the Human Frontiers Science Program (RGP0010/2017). J.H. acknowledges support from the European Development Fund: Structural dynamics of biomolecular systems (ELIBIO) (CZ.02.1.01/0.0/0.0/15_003/ 0000447) EMBO long-term fellowship (ALTF 356-2018) awarded to L.E.F.; the Röntgen-Ångström Cluster (2015-06107 and 2019-06092); the Swedish Research Council (2017-05336, 2018-00234 and 2019-03935); the Swedish Foundation for Strategic Research (ITM17-0455).

Author details

[1]Laboratory of Molecular Biophysics, Department of Cell and Molecular Biology, Uppsala University, Husargatan 3 (Box 596), SE-75124 Uppsala, Sweden. [2]Deutsches Electronen-Synchrotron DESY, Notkestrasse 85, 22607 Hamburg, Germany. [3]European XFEL, Holzkoppel 4, 22869 Schenefeld, Germany. [4]Diamond Light Source, Harwell Science & Innovation Campus, Didcot OX11 0DE, UK. [5]University of Stavanger, Centre Organelle Research, Richard-Johnsensgate 4, 4021 Stavanger, Norway. [6]Leibniz Institute for Experimental Virology (HPI), Centre for Structural Systems Biology, Notkestraße 85, 22607 Hamburg, Germany. [7]Dipartimento di Fisica "Aldo Pontremoli", Università degli Studi di Milano, via Celoria 16, 20133 Milano, Italy. [8]Center for Free-Electron Laser Science, DESY, 22607 Hamburg, Germany. [9]Plant Biology Section, School of Integrative Plant Science, Cornell University, Ithaca, NY 14853, USA. [10]PNSensor GmbH, Otto-Hahn-Ring 6, D-81739 München, Germany. [11]Biomedical and X-Ray Physics, Department of Applied Physics, AlbaNova University Center, KTH Royal Institute of Technology, SE-10691 Stockholm, Sweden. [12]ELI Beamlines/IoP Institute of Physics AS CR, v.v.i., Na Slovance 2, 182 21 Prague 8, Czech Republic. [13]Multi-User CryoEM Facility, Centre for Structural Systems Biology, Notkestr.85, 22607 Hamburg, Germany. [14]University Medical Center Hamburg-Eppendorf (UKE), Martinistrasse 52, 20246 Hamburg, Germany. [15]The Hamburg Center for Ultrafast Imaging, Universität Hamburg, Luruper Chaussee 149, 22761 Hamburg, Germany. [16]Department of Physics, Universität Hamburg, Luruper Chaussee 149, 22761 Hamburg, Germany. [17]Department of Chemistry and Physics, La Trobe Institute for Molecular Science, La Trobe University, Melbourne, VIC 3086, Australia. [18]Division of Scientific Computing, Science for Life Laboratory, Department of Information Technology, Uppsala University, Box 337SE-75105 Uppsala, Sweden. [19]European Molecular Biology Laboratory, c/o DESY, Notkestrasse 85, 22607 Hamburg, Germany. [20]Department of Physics and Astronomy, Uppsala University, Box 516SE-75120 Uppsala, Sweden. [21]Max Planck Institute for the Structure and Dynamics of Matter, Luruper Chaussee 149, 22761 Hamburg, Germany. [22]Center for Free-Electron Laser Science, Luruper Chaussee 149,

22761 Hamburg, Germany. [23]Department of Chemistry, Universität Hamburg, 20146 Hamburg, Germany. [24]NERSC, Lawrence Berkeley National Laboratory, Berkeley, CA 94720, USA

Author contributions

T.E., K.A., H.N.C., Lars.G., J.H., J.K., D.W. and F.R.N.C.M. conceived and designed the experiment. L.A.E., L.H.G., D.H., A.K.S. and P.L.X. prepared and characterised the sample. L.E.F, W.L. and C.S. performed cryo-EM measurements and analysis. J.B., J.K., O.K, J.L., A.P.M., A.K.S. and L.W. developed and operated the sample delivery equipment. D.A., K.A., B.J.D., T.E., D.E.G., Luca.G., A.I., J.K., R.K., F.R.N.C.M., C.N., M.R., E.S., J.A.S., N.T., I.A.V., and T.W. contributed to software development, data processing and analysis. R.B., M.M., T.M., Y.O., D.R., P.S. and S.U. designed and operated the SQS instrument at EuXFEL. R.H., H.Y. and M.K. integrated and operated the pnCCD detector. The manuscript was written by T.E. and F.R.N.C.M. with input from all authors.

Funding

Open access funding provided by Uppsala University.

Data availability

A total of 94,750 detector images were deposited on the Coherent X-ray Imaging Data Bank (CXIDB)[52] under ID 187. This includes sample runs (83,600 images), detector calibration runs (3750 images), runs with only the X-ray beam (1200 images) and X-ray beam, sample delivery gas but without sample (6200 images). The DOI for the original data at the EuXFEL is https://doi.org/10.22003/XFEL.EU-DATA-002146-00.

Code availability

Simulations were performed with the open-source software package Condor[41]. Software to perform the template matching and all auxiliary software for gain correction, and hit finding are available at https://github.com/ekeberg/Ekeberg2022GroEL.

Conflict of interest

The authors declare no competing interests.

Supplementary information The online version contains supplementary material available at https://doi.org/10.1038/s41377-023-01352-7.

Received: 3 November 2023 Revised: 5 December 2023 Accepted: 6 December 2023
Published online: 12 January 2024

References

1. Mankowsky, R. et al. Nonlinear lattice dynamics as a basis for enhanced superconductivity in YBa2Cu3O6.5. *Nature* **516**, 71–73 (2014).
2. Loh, Z. H. et al. Observation of the fastest chemical processes in the radiolysis of water. *Science* **367**, 179–182 (2020).
3. Chapman, H. N. et al. Femtosecond X-ray protein nanocrystallography. *Nature* **470**, 73–77 (2011).
4. Tenboer, J. et al. Time-resolved serial crystallography captures high-resolution intermediates of photoactive yellow protein. *Science* **346**, 1242–1246 (2014).
5. Nogales, E. The development of cryo-EM into a mainstream structural biology technique. *Nat. Methods* **13**, 24–27 (2016).
6. Frank, J. Time-resolved cryo-electron microscopy: recent progress. *J. Struct. Biol.* **200**, 303–306 (2017).
7. Neutze, R. et al. Potential for biomolecular imaging with femtosecond X-ray pulses. *Nature* **406**, 752–757 (2000).
8. Hayer-Hartl, M., Bracher, A. & Hartl, F. U. The GroEL-GroES chaperonin machine: a nano-cage for protein folding. *Trends Biochem. Sci.* **41**, 62–76 (2016).
9. Braig, K. et al. The crystal structure of the bacterial chaperonin GroEL at 2.8 Å. *Nature* **371**, 578–586 (1994).
10. Rostom, A. A. & Robinson, C. V. Detection of the intact groel chaperonin assembly by mass spectrometry. *J. Am. Chem. Soc.* **121**, 4718–4719 (1999).
11. Rose, R. J. et al. High-sensitivity Orbitrap mass analysis of intact macromolecular assemblies. *Nat. Methods* **9**, 1084–1086 (2012).
12. van den Heuvel, R. H. H. et al. Improving the performance of a quadrupole time-of-flight instrument for macromolecular mass spectrometry. *Anal. Chem.* **78**, 7473–7483 (2006).
13. Sobott, F. & Robinson, C. V. Characterising electrosprayed biomolecules using tandem-MS—the noncovalent GroEL chaperonin assembly. *Int. J. Mass Spectrom.* **236**, 25–32 (2004).
14. Roseman, A. M. et al. The chaperonin ATPase cycle: mechanism of allosteric switching and movements of substrate-binding domains in GroEL. *Cell* **87**, 241–251 (1996).
15. Ludtke, S. J. et al. Seeing GroEL at 6 Å resolution by single particle electron cryomicroscopy. *Structure* **12**, 1129–1136 (2004).
16. Seibert, M. M. et al. Single mimivirus particles intercepted and imaged with an X-ray laser. *Nature* **470**, 78–81 (2011).
17. Aquila, A. et al. The linac coherent light source single particle imaging road map. *Struct. Dyn.* **2**, 041701 (2015).
18. Daurer, B. J. et al. Experimental strategies for imaging bioparticles with femtosecond hard X-ray pulses. *IUCrJ* **4**, 251–262 (2017).
19. Ayyer, K. et al. Low-signal limit of X-ray single particle diffractive imaging. *Opt. Express* **27**, 37816–37833 (2019).
20. Ekeberg, T. et al. Three-dimensional reconstruction of the giant mimivirus particle with an x-ray free-electron laser. *Phys. Rev. Lett.* **114**, 098102 (2015).
21. van der Schot, G. et al. Imaging single cells in a beam of live cyanobacteria with an X-ray laser. *Nat. Commun.* **6**, 5704 (2015).
22. Bielecki, J. et al. Electrospray sample injection for single-particle imaging with x-ray lasers. *Sci. Adv.* **5**, eaav8801 (2019).
23. Chapman, H. N. et al. Femtosecond diffractive imaging with a soft-X-ray free-electron laser. *Nat. Phys.* **2**, 839–843 (2006).
24. Tschentscher, T. et al. Photon beam transport and scientific instruments at the european XFEL. *Appl. Sci.* **7**, 592 (2017).
25. Hantke, M. F. et al. Rayleigh-scattering microscopy for tracking and sizing nanoparticles in focused aerosol beams. *IUCrJ* **5**, 673–680 (2018).
26. Kuster, M. et al. The 1-Megapixel pnCCD detector for the Small Quantum Systems Instrument at the European XFEL: system and operation aspects. *J. Synchrotron Radiat.* **28**, 576–587 (2021).
27. Strüder, L. et al. Large-format, high-speed, X-ray pnCCDs combined with electron and ion imaging spectrometers in a multipurpose chamber for experiments at 4th generation light sources. *Nucl. Instrum. Methods Phys. Res. Sect. A: Accel. Spectrom. Detect. Assoc. Equip.* **614**, 483–496 (2010).
28. Decking, W. et al. A MHz-repetition-rate hard X-ray free-electron laser driven by a superconducting linear accelerator. *Nat. Photonics* **14**, 391–397 (2020).
29. Chaudhry, C., Horwich, A. L., Brunger, A. T. & Adams, P. D. Exploring the structural dynamics of the *E. coli* chaperonin GroEL using translation-libration-screw crystallographic refinement of intermediate states. *J. Mol. Biol.* **342**, 229–245 (2004).
30. Hogan, C. J. et al. Tandem differential mobility analysis-mass spectrometry reveals partial gas-phase collapse of the GroEL complex. *J. Phys. Chem. B* **115**, 3614–3621 (2011).
31. Marklund, E. G., Larsson, D. S. D., van der Spoel, D., Patriksson, A. & Caleman, C. Structural stability of electrosprayed proteins: temperature and hydration effects. *Phys. Chem. Chem. Phys.* **11**, 8069–8078 (2009).
32. Esser, T. K. et al. Cryo-EM of soft-landed β-galactosidase: Gas-phase and native structures are remarkably similar. Preprint at *BioRxiv* https://doi.org/10.1101/2023.08.17.553673 (2023).
33. Hau-Riege, S. P. et al. Sacrificial tamper slows down sample explosion in FLASH diffraction experiments. *Phys. Rev. Lett.* **104**, 064801 (2010).
34. Maia, F. R. N. C., Ekeberg, T., Timneanu, N., van der Spoel, D. & Hajdu, J. Structural variability and the incoherent addition of scattered intensities in single-particle diffraction. *Phys. Rev. E* **80**, 031905 (2009).
35. Porro, M. et al. The MiniSDD-based 1-Megapixel Camera of the DSSC Project for the European XFEL. *IEEE Trans. Nucl. Sci.* **68**, 1334–1350, https://doi.org/10.1109/TNS.2021.3076602 (2021).
36. Gessler, P. et al. Overview of acquisition and control electronics and concepts for experiments and beam transport at the European XFEL. In *Proceedings of the 17th Biennial International Conference on Accelerator and Large Experimental Physics Control Systems*. New York, https://doi.org/10.18429/jacow-icalepcs2019-thapp05 (2020).
37. Motuk, E. et al. Design and development of electronics for the EuXFEL clock and control system. *J. Instrum.* **7**, C01062 (2012).
38. Maltezopoulos, T. et al. Operation of X-ray gas monitors at the European XFEL. *J. Synchrotron Radiat.* **26**, 1045–1051 (2019).

39. Daurer, B. J., Hantke, M. F., Nettelblad, C. & Maia, F. R. N. C. Hummingbird: monitoring and analyzing flash X-ray imaging experiments in real time. *J. Appl. Crystallogr.* **49**, 1042–1047 (2016).
40. Abraham, M. J. et al. GROMACS: High performance molecular simulations through multi-level parallelism from laptops to supercomputers. *SoftwareX* **1–2**, 19–25 (2015).
41. Hantke, M. F., Ekeberg, T. & Maia, F. R. N. C. Condor: a simulation tool for flash X-ray imaging. *J. Appl. Crystallogr.* **49**, 1356–1362 (2016).
42. Loh, N.-T. D. & Elser, V. Reconstruction algorithm for single-particle diffraction imaging experiments. *Phys. Rev. E* **80**, 026705 (2009).
43. Virtanen, P. et al. SciPy 1.0: fundamental algorithms for scientific computing in Python. *Nat. Methods* **17**, 261–272 (2020).
44. Freeke, J., Robinson, C. V. & Ruotolo, B. T. Residual counter ions can stabilise a large protein complex in the gas phase. *Int. J. Mass Spectrom.* **298**, 91–98 (2010).
45. Zivanov, J. et al. New tools for automated high-resolution cryo-EM structure determination in RELION-3. *eLife* **7**, e42166 (2018).
46. Punjani, A. et al. cryoSPARC: algorithms for rapid unsupervised cryo-EM structure determination. *Nat. Methods* **14**, 290–296 (2017).
47. Zheng, S. Q. et al. MotionCor2: anisotropic correction of beam-induced motion for improved cryo-electron microscopy. *Nat. Methods* **14**, 331–332 (2017).
48. Zhang, K. Gctf: real-time CTF determination and correction. *J. Struct. Biol.* **193**, 1–12 (2016).
49. Roh, S.-H. et al. Subunit conformational variation within individual GroEL oligomers resolved by Cryo-EM. *Proc. Natl Acad. Sci. USA* **114**, 8259–8264 (2017).
50. Pettersen, E. F. et al. UCSF Chimera—a visualization system for exploratory research and analysis. *J. Comput. Chem.* **25**, 1605–1612 (2004).
51. Wagner, T. et al. SPHIRE-crYOLO is a fast and accurate fully automated particle picker for cryo-EM. *Commun. Biol.* **2**, 218 (2019).
52. Maia, F. R. N. C. The Coherent X-ray Imaging Data Bank. *Nat. Methods* **9**, 854–855 (2012).
53. Wiedorn, M. O. et al. Post-sample aperture for low background diffraction experiments at X-ray free-electron lasers. *J. Synchrotron Radiat.* **24**, 1296–1298 (2017).